Thermal-dephasing-tolerant generation of mesoscopic superposition states with Rydberg dressed blockade

Ri-Hua Zheng,[1] S.-L. Su,[2,*] Jie Song,[3] Weibin Li,[4,†] and Yan Xia[1,‡]

[1]*Fujian Key Laboratory of Quantum Information and Quantum Optics, College of Physics and Information Engineering, Fuzhou University, Fuzhou, Fujian 350108, China*

[2]*School of Physics, Zhengzhou University, Zhengzhou 450001, China*

[3]*Department of Physics, Harbin Institute of Technology, Harbin 150001, China*

[4]*School of Physics and Astronomy, University of Nottingham, Nottingham NG7 2RD, United Kingdom*

(Received 11 January 2023; accepted 14 September 2023; published 4 October 2023)

Multipartite entangled states involving nonlocality are one of the most fascinating characteristics of quantum mechanics. In this work we propose a thermal-dephasing-tolerant generation of mesoscopic entangled states with Rydberg dressed atoms. We encode a logical state on dressed states rather than Rydberg states. Such treatment can increase the lifetime of multipartite entanglement coherence to around three times compared to the Rydberg-state-coding one at the same system size and therefore induce solid fidelities of mesoscopic superposition states generation. The current work theoretically verifies the advantages of using Rydberg dressed states in many-body quantum entanglement, which is helpful for large-scale quantum computation and many-body Rydberg quantum simulation.

DOI: 10.1103/PhysRevA.108.042405

I. INTRODUCTION

Rydberg atoms exhibit very strong van der Waals interactions [1], which can be flexibly modulated by varying the interatomic distances and therefore show great potential in the quantum simulations of many-body systems [2–5]. Many applications based on Rydberg atoms rely on the ability to coherently manipulate atoms on timescales below the radiation lifetime of the excited state. Interestingly, it has been found [6–8] that weakly admixing excited Rydberg states with laser light can extend this timescale limitation. This proposal can also be utilized to produce a novel type of long-range interactions between Rydberg dressed ground-state atoms [9,10], which provides a tool to enhance coherence of many-body systems from inelastic collisions and spontaneous emission, such as the production of exotic quantum phases [7,9,11], spin squeezing [8,12], quantum computation [13,14], and entanglement generation [15–19].

Multipartite entanglement lies at the heart of many-body quantum simulation. Among diverse types of entangled states, the Greenberger-Horne-Zeilinger (GHZ) states [20] (or called two-component atomic cat states [21,22]) have attracted a lot of research interest [23–25] because of their characteristics of maximum entanglement. Recently, two experimental works [26,27] simultaneously report the generation of 20-qubit GHZ states with similar fidelity $\mathcal{F} \sim 0.55$ on the Rydberg atoms platform and the superconducting qubits platform, respectively. One of the major obstacles to achieving higher fidelity for generating multipartite entanglement [26], as well as other extensive quantum simulation and quantum computation based on Rydberg atoms [28–36], is thermal dephasing. Due to the finite temperature of neutral atoms, the Doppler shift occurs on each site of the Rydberg atom arrays [26,37]. Additionally, the thermal noise causes fluctuations of atomic distance (for example, $\delta R/R \sim 6\%$ [28]), i.e., disturbing the desired electric dipole-dipole interaction (EDDI) strength. The above two disturbances together constitute the thermal dephasing mechanisms, which have hindered the high-precision completion of many quantum works [26,28,29] with Rydberg atoms. Especially when multiple Rydberg atoms are excited to Rydberg states, the thermal dephasing, quantified by the lifetime of coherence T_2, becomes shorter with the increase in the number of atoms N (specifically, $T_2 \sim 0.6$ μs for $N = 20$ [26]). Therefore Rydberg dressing is a promising candidate to solve these problems caused by thermal dephasing.

In this work we propose to generate mesoscopic superposition states through a Rydberg-dressing-induced blockade. We dress the Rydberg atom probability to $P_r = 25\%$, leading to coherence lifetimes of $T_2 = \{11.0, 8.2, 7.2, 6.2, 5.7, 5.1\}$ μs for {4, 6, 8, 10, 12, 14}-atom GHZ states, around three times that of T_2 in the work of Ref. [26], at the same system size. For larger-scale systems, the dressed lifetime T_2 decreases with the system size N as $1/\sqrt{N}$, which is the same as the scaling rule in the work without Rydberg dressing [26]. The fidelities are {97.2%, 95.1%, 91.1%, 84.6%} for {4, 6, 8, 10}-atom GHZ states when considering the thermal dephasing. Based on the above fidelities data, we give a prediction fidelity of 80% for the 20-atom GHZ state. The balance between dressing low-percentage Rydberg states and shortening the evolution time in large-scale neutral atoms systems in

*slsu@zzu.edu.cn

†weibin.Li@nottingham.ac.uk

‡xia-208@163.com

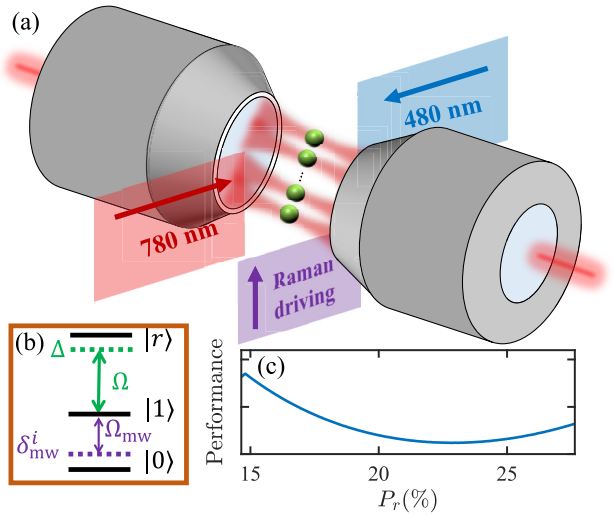

FIG. 1. (a) Envisioned experimental setup. All atoms fixed on the one-dimensional array are driven by Rydberg dressed lasers (780 and 480 nm) and Raman (microwave) drivings with the same detunings and Rabi frequencies. Two addressing lasers (not shown) are added on the two edge atoms to differentiate microwave detunings from other atomic ones. (b) Energy levels and couplings of each atom. (c) Performance of the entanglement generation vs dressed percentage P_r. This performance index combines the impact of the lifetime, dressed interaction, and dressed interaction bandwidth (see the text for details).

the present work may provide a reference for quantum computation and quantum simulation based on multiple dressed atoms. The Rydberg-dressing method for many-body entanglement generation is scalable and dephasing-tolerant, which will contribute to realizing near-term quantum simulation and quantum computation with Rydberg atom arrays, such as entanglement-enhanced sensing [38], quantum metrology [39], and quantum error correction [40] based on GHZ states.

The article is organized as follows. In Sec. II we give the physical model for the generation of multipartite entanglements with the Rydberg dressing. In Sec. III we discuss the main causes of the thermal dephasing in Rydberg atoms. Scaling of fidelities and T_2 are placed in Secs. IV and V, respectively. The conclusion is given in Sec. VI.

II. PHYSICAL MODEL

Consider a one-dimensional array with an even number N of neutral ^{87}Rb atoms trapped in the optical tweezers, as shown in Fig. 1. For all the atoms we encode two ground states $|0\rangle = |5S_{1/2}, F = 1, m_F = 1\rangle$ and $|1\rangle = |5S_{1/2}, F = 2, m_F = 2\rangle$ and one excited Rydberg state $|r\rangle = |70S, J = 1/2, m_J = -1/2\rangle$ [26,41]. The coupling between $|1\rangle$ and $|r\rangle$ is driven by a two-photon transition with effective coupling strength Ω and detuning Δ. Additionally, the microwave-frequency fields with strength $\Omega_{\rm mw}(t)$ and detuning $\delta^n_{\rm mw}(t)$ are added for driving the rotations between the ground states $|0\rangle$ and $|1\rangle$. We choose the nearest-neighbor EDDI energy, $V/(2\pi) = 21$ MHz, i.e., equal adjacent atomic intervals of 5.87 μm and $C_6 = 858\,\text{GHz}\,\mu\text{m}^6$ h. The Hamiltonian here is given by ($\hbar = 1$ and $n, i, j \leqslant N$)

$$H = H_{\rm RDB} + H_{\rm mw}, \tag{1a}$$

$$H_{\rm RDB} = \sum_{n=1}^{N} \frac{\Omega}{2}\sigma^n_{x,r1} + \Delta\sigma^n_{rr} + \sum_{i<j} \frac{V}{|i-j|^6}\sigma^i_{rr}\sigma^j_{rr}, \tag{1b}$$

$$H_{\rm mw} = \sum_{n=1}^{N} [\Omega_{\rm mw}(t)\sigma^n_{x,0d} + \left[U_1 - \delta^n_{\rm mw}(t)\right]\sigma^n_{00}, \tag{1c}$$

with $\sigma^n_{\alpha\alpha} = |\alpha\rangle_n\langle\alpha|$, $\sigma^n_{x,\alpha\beta} = |\alpha\rangle_n\langle\beta| + |\beta\rangle_n\langle\alpha|(\alpha = r, 0;\ \beta = 1, d)$, where $|d\rangle$ is the dressed state, given by $|d\rangle = -\text{sgn}(\Delta)\sin(\theta/2)|1\rangle + \cos(\theta/2)|r\rangle$, with $\sin\theta = \Omega/\sqrt{\Omega^2+\Delta^2}$ and $\cos\theta = -\text{sgn}(\Delta)\Delta/\sqrt{\Omega^2+\Delta^2}$. Therefore the percentage P_r of Rydberg states in the dressed states is $\cos^2(\theta/2)$. Note the driving between $|0\rangle$ coupling $|r\rangle$ is also a two-photon transition. For each pair of adjacent atoms, after abandoning decoupled antisymmetric state $(|1r\rangle - |r1\rangle)/\sqrt{2}$, the Hamiltonian can be reduced to

$$H^{(2)}_{\rm RDB} = \begin{pmatrix} 0 & \frac{\Omega}{\sqrt{2}} & 0 \\ \frac{\Omega}{\sqrt{2}} & \Delta & \frac{\Omega}{\sqrt{2}} \\ 0 & \frac{\Omega}{\sqrt{2}} & 2\Delta + V \end{pmatrix}, \tag{2}$$

in basis $\{|11\rangle, (|1r\rangle + |r1\rangle)/\sqrt{2}, |rr\rangle\}$. Equation (2) is insightful in that it allows us to understand the energy scales directly.

The performance of the entanglement generation is quantified as per. $= JT_2\text{bw}_J$, shown in Fig. 1(c) with free units, where J and bw_J are the dressed energy and dressed energy bandwidth, respectively. The dressed energy, arising from the Stark shifts caused by the reciprocity among the EDDI and dressed laser drivings, is given by $J = |2U_1 - U_2|$, with $U_1 = (\Delta - \text{sgn}(\Delta)\sqrt{\Omega^2+\Delta^2})/2$ and $U_2 = -\text{sgn}(\Delta)\min|\text{eig}(H^{(2)}_{\rm RDB})|$ representing single- and double-atom Stark shifts on the dressed states, respectively. When the Rydberg blockade effect is strong enough ($V \gg \{\Omega, \Delta\}$), one can calculate that $U_2 = [\Delta - \text{sgn}(\Delta)\sqrt{2\Omega^2+\Delta^2}]/2$, which coincides with the results in [9,10,17]. For illumination we plot the dressed energy J versus detuning Δ and EDDI strength V in Fig. 2.

As exhibited in Fig. 2, the stick-shaped area around the green dashed line processes higher dressed energy J. This area demonstrates an interesting physical phenomenon called the Rydberg antiblockade [42–47]. In principle, in all the regions of Fig. 2, the dressed energy J on the two-atom dressed states $|dd\rangle_{i(i+1)}$ blockade the associated transitions from the ground state to $|dd\rangle_{i(i+1)}$ [adjusting $J \gg \Omega_{\rm mw}$, dropping (t) hereafter]. That is another phenomenon with rich physical connotations, called a Rydberg dressed blockade (RDB) [8–10,17–19], which acts like the Rydberg blockade, however with a difference that the transitions to adjacent atoms in the dressed state $|dd\rangle_{i(i+1)}$ rather than the two-atom Rydberg states $|rr\rangle_{i(i+1)}$ are forbidden.

To shorten the evolution time of the dynamics induced by $H_{\rm mw}$, we prefer a larger dressed energy J for RDB. On the other hand, to reduce the thermal dephasing of atoms, the composition of Rydberg states P_r should be small (resisting atomic Doppler shifts). Additionally, the dressed

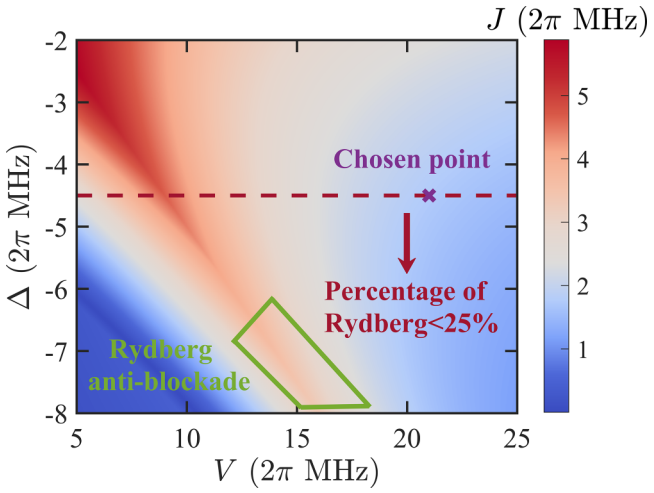

FIG. 2. Dressed energy J vs detuning Δ and EDDI strength V. The effective coupling strength Ω is fixed at $2\pi \times 8$ MHz. The area where the percentage of Rydberg states P_r is less than 25% is marked below the red dotted line. The stick-shaped area represents the Rydberg antiblockade with weak regimes (not satisfying $\Delta \gg \Omega$). The selected point $(V, \Delta)/(2\pi) = (21, -4.5)$ MHz is marked by a cross.

energy J needs to be stable within a certain fluctuation range of V (resisting atomic position floating). Ergo, we choose $(V, \Delta)/(2\pi) = (21, -4.5)$ MHz with $P_r = 25\%$.

Until now, the light shift (caused by the dressed laser) for each atom can be canceled by the $U_1|0\rangle_n\langle 0|$ term of the Hamiltonian of microwave-frequency fields, $H_{\rm mw}$. Then we use $H_{\rm mw}$ to flexibly manipulate the dynamics of multiple atoms in subspace $\mathcal{S}_1 = \{|0\rangle, |d\rangle\}$ (equal to an N-qubit quantum system). Moreover, due to the RDB effect, the subspace $\mathcal{S}_2 = \{|dd\rangle_{i(i+1)}\}$ are forbidden. The calculation space is further locked into $\mathcal{S}_3 = \complement_{\mathcal{S}_1}\mathcal{S}_2$. Therefore we successfully reduce the calculation dimension of the N-qubit quantum system from 2^N to $\sum_{m=0}^{N/2} C_{N+1-m}^m$ (see Appendix A for details), analogous to the multiple-qubit work by Omran *et al*. [26]. Remarkably, such a reduction of the dimension of the system subspace induces a nonlocal effect to generate entanglement [17,26]. Since the dynamics of the full Hilbert space and the reduced space are not completely equivalent, we use the projection ratio $\mathcal{P}_N = {\rm Tr}_{\mathcal{S}_2}\rho_f$ of the N-atom reduced subspace relative to the corresponding full Hilbert space as a benchmark for the divergence between them. For the systems with $N = 4, 6, 8, 10, 12$, we obtain $\mathcal{P}_N = 0.98, 0.95, 0.95, 0.93, 0.90$.

Further, by appropriately adjusting the addressing drivings applied on edge atoms, we can make their microwave detunings ($\delta_{\rm mw}^e$) different from other atomic ones ($\delta_{\rm mw}^{ne}$), i.e., $\delta_{\rm mw}^1 = \delta_{\rm mw}^N = \delta_{\rm mw}^e \neq \delta_{\rm mw}^p = \delta_{\rm mw}^{ne}$ ($p = 2, 3, ..., N-1$). When $\delta_{\rm mw}^e$ is closed to $\delta_{\rm mw}^{ne}$ but differs in certain values, the initial state $|0000\cdots\rangle$ will be driven to the GHZ state $|{\rm GHZ}_N\rangle = (|d0d0\cdots d0\rangle + |0d0d\cdots 0d\rangle)/\sqrt{2}$ by adiabatically increasing detuning ($-\delta_{\rm mw}^n$) from negative large values to positive large values (see Appendix B for deviations). Such an adiabatic method has been proved in the work of Ref. [26], and they optimize their pulses through a remote dressed chopped-random-basis algorithm [48,49]. Here we utilize another effective optimal control method, gradient ascent pulse engineering (GRAPE) [50] (recently proved to be a precise algorithm in the experiment [51–54]), to shorten the evolution time of the above adiabatic process for the multipartite GHZ states generation. The optimization results are exhibited in Table I. Note that the maximum absolute value of $\Omega_{\rm mw}$ does not exceed $2\pi \times 0.14$ MHz to ensure the stability of the RDB dynamics ($J \gg \Omega_{\rm mw}$). Detailed driving pulses for {4, 6, 8, 10}-atom systems can be seen in Appendix C.

TABLE I. Ideal fidelities and preparation times optimized by the GRAPE. The ideal fidelity is calculated in the effective subspace $\mathcal{S}_3$ (no $\{|dd\rangle_{i(i+1)}\}$ subspace).

Number of atoms	Time (μs)	Ideal fidelity
4	2.1	0.99
6	3.1	0.99
8	4.2	0.99
10	5.3	0.99
12	5.9	0.99
14	7.6	0.99
16	8.3	0.99

III. THERMAL DEPHASING

We next consider a very critical experimental imperfection, the thermal dephasing noise, in the numerical simulation. The finite temperature of atoms induces their nonzero spread velocity and position uncertainty. Such that the thermal dephasing mechanism is determined by these two factors.

(i) The position uncertainty can be modeled by the Gaussian distribution with the probability density function being $\mathcal{N}(x_n, \sigma^2) = e^{-(x-x_n)^2/(2\sigma^2)}/(\sqrt{2\pi}\sigma)$, where x_n is the ideal position of the nth atom and σ^2 is the variance. The adjacent distance of the atoms is $R = \mathcal{N}(x_i, \sigma^2) - \mathcal{N}(x_{i+1}, \sigma^2) = \mathcal{N}(R_0, 2\sigma^2)$ with $R_0 = x_i - x_{i+1} = 5.87$ μm. Specifically, the standard deviation σ of Gaussian distribution for an atom in a finite temperature ~10 μK is around 0.1 μm [26,55]. As $V = C_6/R^6$, a spread in interaction strength can be calculated by the position distribution and further simulated with the original Hamiltonian in Eq. (1).

(ii) The spread velocity causes fluctuating Doppler shifts. According to concrete reports [37,56,57], the Doppler shift leads to a random detuning δ^D on each atom-array site, viz., $\delta^D \in \mathcal{N}(0, \sigma_D^2)$, simulated as an error term $H^D = \delta^D|r\rangle\langle r|$ added to the original Hamiltonian in Eq. (1). The value of σ^D is given by $\sigma^D = k_{\rm eff}\Delta v$, with $k_{\rm eff} = |\boldsymbol{k}_{|1\rangle\leftrightarrow|e\rangle} + \boldsymbol{k}_{|e\rangle\leftrightarrow|r\rangle}|$ the effective wave vector of two-photon transition $|1\rangle \leftrightarrow |r\rangle$ and $\Delta v = \sqrt{k_B T/m}$ the one-dimensional rms velocity spread of atoms. Bringing in the values of Boltzmann constant k_B, atomic temperature $T = 10$ μK [26], and atomic mass $m = 87 \times 1.66 \times 10^{-27}$ kg, we can give the rms velocity spread $\Delta v = \sqrt{k_B T/m} = 0.031$ m/s. On the other hand, one can drive $|1\rangle \leftrightarrow |e\rangle$ ($|e\rangle \leftrightarrow |r\rangle$) by a 780-nm (480-nm) laser with $|\boldsymbol{k}_{|1\rangle\leftrightarrow|e\rangle}| = 2\pi/780$ nm^{-1} ($|\boldsymbol{k}_{|e\rangle\leftrightarrow|r\rangle}| = 2\pi/480$ nm^{-1}). These two lasers can be focused on the atom array by opposite directions [37] to minimize the Doppler shifts, resulting in $k_{\rm eff} = 2\pi/480$ nm$^{-1} - 2\pi/780$ nm^{-1} and further $\sigma_D/(2\pi) = 24.77$ kHz. Since the energy of ground states $|0\rangle$ and $|1\rangle$ is closed, the Doppler shifts are almost the same for $|1\rangle \leftrightarrow |r\rangle$

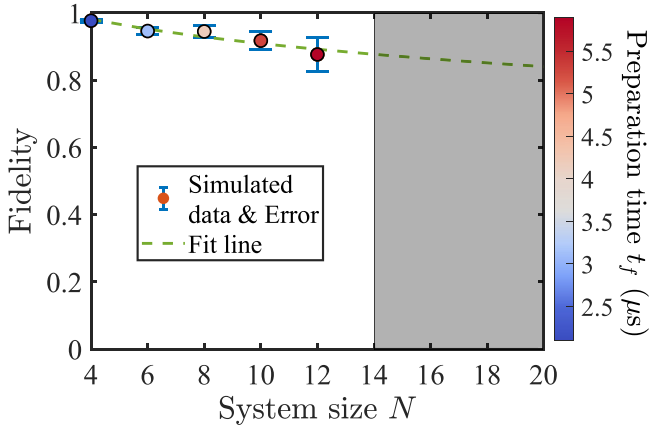

FIG. 3. Fidelities of GHZ states in the systems at different scales. The colors of dots scale the corresponding preparation time for GHZ states. The green dashed line exhibits the fitting results [based on $\ln(\mathcal{F}-1/2)\propto-\sqrt{N}$] induced from the fidelities for {4, 6, 8, 10, 12}-atom systems. This line gives a prediction of the fidelities for larger $N\geqslant 14$ and also more difficult to compute systems marked by a gray area.

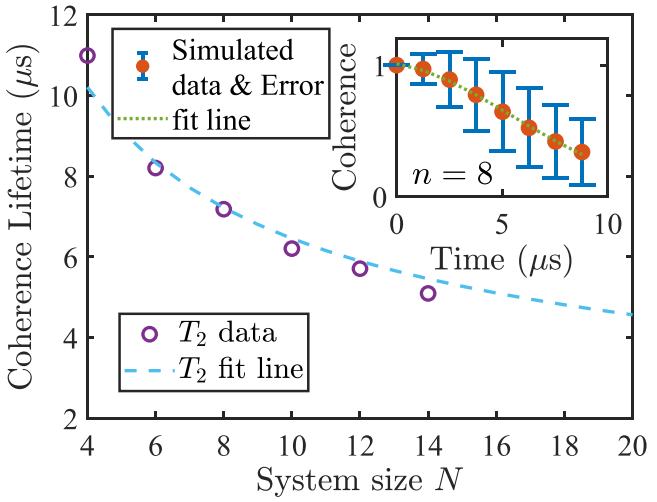

FIG. 4. Coherence lifetime (T_2) vs system size N. The circles show the T_2 data inferred by Gaussian fittings of the coherence damping for systems with different sizes, and the blue dashed line gives a predicted trend ($T_2\propto 1/\sqrt{N}$) for larger systems ($N\geqslant 16$). As an example, the inset exhibits the coherence damping of an eight-atom system with a green dotted line obeying Gaussian fitting. Similar to Fig. 3, the dots and error bars are mean values and standard deviations of coherence.

and $|0\rangle\leftrightarrow|r\rangle$. Therefore the error term $H^D=\delta^D|r\rangle\langle r|$ can well describe the Doppler shifts effect in the present atomic systems.

IV. SCALING OF FIDELITIES

Considering the above two negative factors, the simulation results for GHZ states preparation in {4, 6, 8, 10}-atom systems are shown in Fig. 3. The full Hamiltonian in Eq. (1) is utilized to calculate the fidelities for {4, 6, 8, 10}-atom systems. The thermal dephasing (including the position uncertainty and the Doppler shifts) is considered during the numerical simulation by repeatedly calculating fidelities based on different values of R and δ^D (obeying the normal distribution), which induces the error bars (standard deviation) in Fig. 3. For each simulated final density matrix ρ_f, we deduce fidelity $\mathcal{F}=\langle \mathrm{GHZ}_N|\rho_f|\mathrm{GHZ}_N\rangle=\frac{1}{2}(p_{A_N}+p_{\bar{A}_N}+c_N+c_N^*)$ [26], where $p_{A_N}(p_{\bar{A}_N})$ is population on $|A_N\rangle=|d0d0\cdots d0\rangle$ ($|\bar{A}_N\rangle=|0d0d\cdots 0d\rangle$) and $c_N=\langle\bar{A}_N|\rho_f|A_N\rangle$ describes the coincidence of off-diagonal terms. The fidelity of the four-atom GHZ state is higher than 97%. Even in the 10-atom system, the fidelity is still close to 85%. Additionally, according to the prediction line in Fig. 3, the fidelity of the 20-atom system will be around 80%.

V. SCALING OF T_2

To further benchmark the dephasing effect of present dressed-atom systems, we assume the initial state is $|\mathrm{GHZ}_N\rangle$ and turn off all the driving lases for a specific time τ and calculate the corresponding density matrix $\rho'(\tau)$. By counting $2|\langle\bar{A}_N|\rho'(\tau)|A_N\rangle|$ as the coherence and defining the coherence lifetime T_2 satisfying $2|\langle\bar{A}_N|\rho'(T_2)|A_N\rangle|=e^{-1}$, we show T_2 versus system size N in Fig. 4. These T_2 data are around 3 times that of the observed data in the previous work [26] without dressing atoms, at the same system size.

The above results come from the current cooling limited temperature $T=10$ μK of cold atoms [4,26]. In the future, with the development of experimental techniques, the atoms may be cooled to lower temperatures. We here give an estimate of fidelity $\mathcal{F}$ versus atomic temperature T to show the prospect of our scheme, with the simulation results of {4, 6, 8, 10}-atom systems shown in Fig. 5. The relationship between fidelity $\mathcal{F}$ and decoherence time T_2 is $\ln(\mathcal{F}-1/2)\propto-1/T_2$. The coherence T_2 results from the thermal motion described by the Boltzmann distribution and therefore satisfies $T_2\propto 1/\sqrt{T}$. The final relationship between fidelity $\mathcal{F}$ and atomic temperature T is $\ln(\mathcal{F}-1/2)\propto-\sqrt{T}$, which coincides well

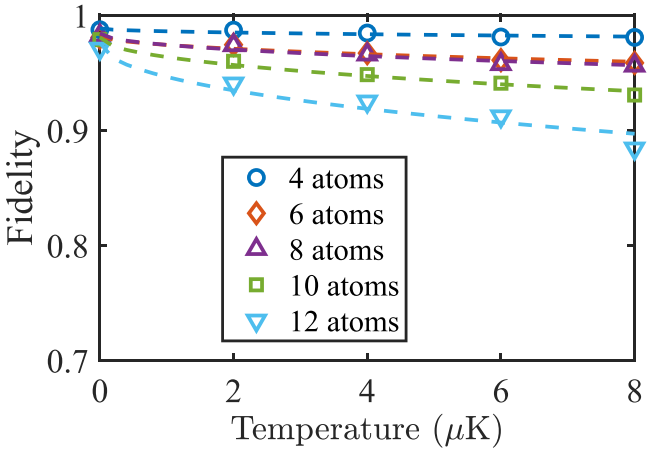

FIG. 5. Fidelities of GHZ states vs atomic temperature. The circles, diamonds, triangles, and squares represent the fidelity of {4, 6, 8, 10, 12}-atom GHZ states, respectively. The dash lines correspondingly show the fitting results based on $\ln(\mathcal{F}-1/2)\propto-\sqrt{T}$ for different scale systems.

with the simulation results in Fig. 5, and also gives prediction that the fidelities of {4, 6, 8, 10, 12}-atom GHZ states can reach above 90% when the atomic temperature is lower than 10 μK.

It is worth noting that the Rydberg state percentage P_r of the dressed state is 25%. According to the lifetime of 70S Rydberg state of 146 μs [37,58], the lifetime of the dressed state could extend to 573 μs, long enough to ignore the depopulation effect factor as the preparation times of GHZ states around 10 μs. Additionally, we only consider the near-neighbor and next-neighbor interactions.

VI. CONCLUSION

We have explored the thermal-dephasing-tolerant generation of GHZ states in dressed-atom systems. The thermal dephasing is suppressed here to 1/3 of the original performance in multibody entangled systems [26], leading to solid fidelities of multibody GHZ states. As the dephasing factor becomes an important obstacle to large-scale quantum computation and quantum simulation based on neutral atoms, the present work may be referable to building dephasing-tolerant quantum tasks in large-scale systems. Combining the Rydberg dressed state method with GPAPE optimal control techniques also provides an enlightening new perspective for robust handling of many-body Rydberg quantum simulations and quantum computation.

ACKNOWLEDGMENTS

This work was supported by the National Natural Science Foundation of China under Grants No. 11575045, No. 11874114, No. 11674060, and No. 11805036; the Natural Science Funds for Distinguished Young Scholar of Fujian Province under Grant No. 2020J06011; and by Fuzhou University under Grant No. JG202001-2. S.L.S. acknowledges support from National Natural Science Foundation of China under Grant No. 12274376 and a major science and technology project of Henan Province under Grant No. 221100210400. W.L. acknowledges support from the EPSRC through Grant No. EP/W015641/1 and the British Council through an Industry Academia Collaborative Grant (No. IND/CONT/G/22-23/26).

APPENDIX A: CALCULATION DIMENSION REDUCTION THROUGH THE RYDBERG DRESSED BLOCKADE

In the main text we use $H_{\rm mw}$ to manipulate the dynamics of multiple atoms in subspace $\mathcal{S}_1 = \{|0\rangle, |d\rangle\}$. Further, the subspace $\mathcal{S}_2 = \{|dd\rangle_{i(i+1)}\}$ are forbidden because of the Rydberg dressed blockade (RDB) effect. Therefore, the calculation space is locked to $\mathcal{S}_3 = \complement_{\mathcal{S}_1}\mathcal{S}_2$, with the calculation dimension reduced from 2^N to $\sum_{m=0}^{N/2} C_{N+1-m}^{m}$ (see Fig. 6).

APPENDIX B: ADIABATIC PASSAGE FOR THE GHZ STATES GENERATION

In the subspace $\mathcal{S}_2$ restricted by the RDB, there are at most $N/2$ atoms in dressed states, when the detuning $-\delta_{\rm mw}^{n}$ represents large negative values (compare to $\Omega_{\rm mw}$), and the system ground state is clearly $|0000\cdots\rangle$. When $-\delta_{\rm mw}^{n}$ represents large positive values, the system ground state becomes degenerate, with $N/2+1$ states with $N/2$ dressed-state excitations, for example, ground states $\{|d00d\rangle, |0d0d\rangle, |d0d0\rangle\}$ when $N=4$ and $\{|d0d00d\rangle, |d00d0d\rangle, |0d0d0d\rangle, |d0d0d0\rangle\}$ when $N=6$. Further, by differing the detuning $-\delta_{\rm mw}^{n}$ between the edge atoms and other atoms, one can separate such degenerate ground states with energy $\delta^{d}/(2\pi) = (\delta_{\rm mw}^{e} - \delta_{\rm mw}^{ne})/(2\pi) = 0.5\,\text{MHz}$. Subsequently, the ground state when $-\delta_{\rm mw}^{n}$ represents large positive values becomes only the GHZ state $|\text{GHZ}_N\rangle$. That is why we can adiabatically change the detuning $-\delta_{\rm mw}^{n}$ from large negative values to large positive values to prepare the GHZ states from the initial state $|0000\cdots\rangle$. For visualization, we have drawn the diagram of adiabatic passages for systems with different sizes in Fig. 7. Such an adiabatic method has been proved in the work of Ref. [26].

APPENDIX C: GRAPE-OPTIMIZED PULSES FOR THE GHZ STATE GENERATION

The optimized method we used is call gradient ascent pulse engineering (GRAPE) [50]. We preset the control Hamiltonians as $H_h = |0\rangle_h\langle 0| + |0\rangle_{N+1-h}\langle 0|$ $(h = 1, 2, ..., N/2)$. The corresponding control pulses are set as $f_h = \delta_{\rm mw}^{h}$. The detailed derivation can be found in Ref. [50], and here we only give the specific optimization steps:

(1) Guess the initial microwave pulses $\Omega_{\rm mw} = 0.14\,\text{MHz}$, $f_{h\neq 1} = (10\Omega_{\rm mw} t/t_f - 5\Omega_{\rm mw})$, and $f_1 = f_{h\neq 1} - 1.25\Omega_{\rm mw}$, where t is the evolution time and t_f is the final evolution time dependent on the system size N.

(2) Calculate the evolution operator $U(t)$.

(3) Change the new control pulses as $f_h' = f_h - i\epsilon_h \cdot \Delta t \cdot \text{Tr}\{[H_k, U(t)\rho_0 U(t)^\dagger] \cdot U(t)U(t_f)^\dagger \rho_f U(t_f)U(t)^\dagger\}$, with ρ_f the desired state, i.e., the GHZ state. Here $\epsilon_h = \Omega_{\rm mw}/2$

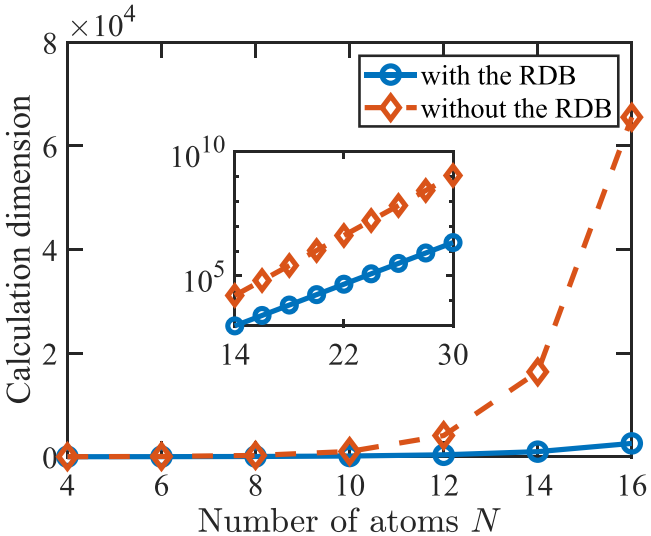

FIG. 6. Calculation dimension vs the number of atoms N (a) with RDB and (b) without RDB effects. The inset shows the case of logarithmic coordinates when $N \in [14, 30]$.

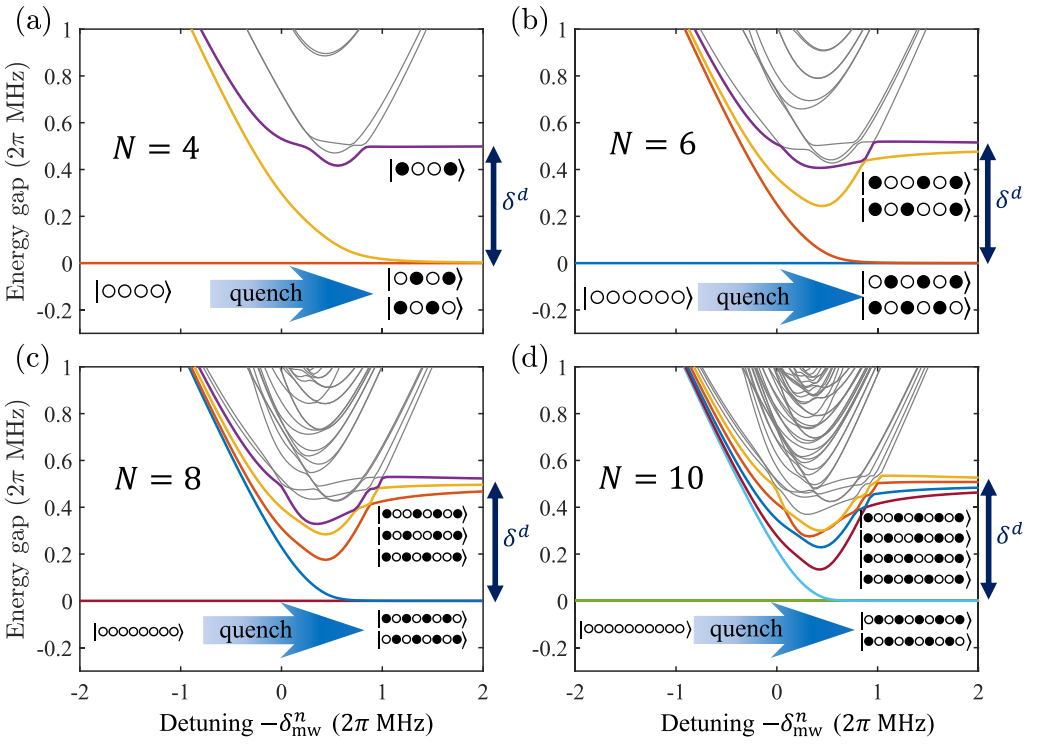

FIG. 7. Energy gaps vs the microwave detuning $-\delta^n_{\rm mw}$ for the system size (a) $N = 4$, (b) $N = 6$, (c) $N = 8$, and (d) $N = 10$. We choose $\Omega_{\rm mw}/(2\pi) = 0.2$ MHz and $(\delta^e_{\rm mw} - \delta^{ne}_{\rm mw})/(2\pi) = \delta^d/(2\pi) = 0.5$ MHz. Formats $|\circ\rangle$ and $|\bullet\rangle$ represent $|0\rangle$ and $|d\rangle$ for visual intuition, respectively. Some unimportant eigenstates are plotted as gray. This graph refers to the presentation form in Ref. [26] with data differences.

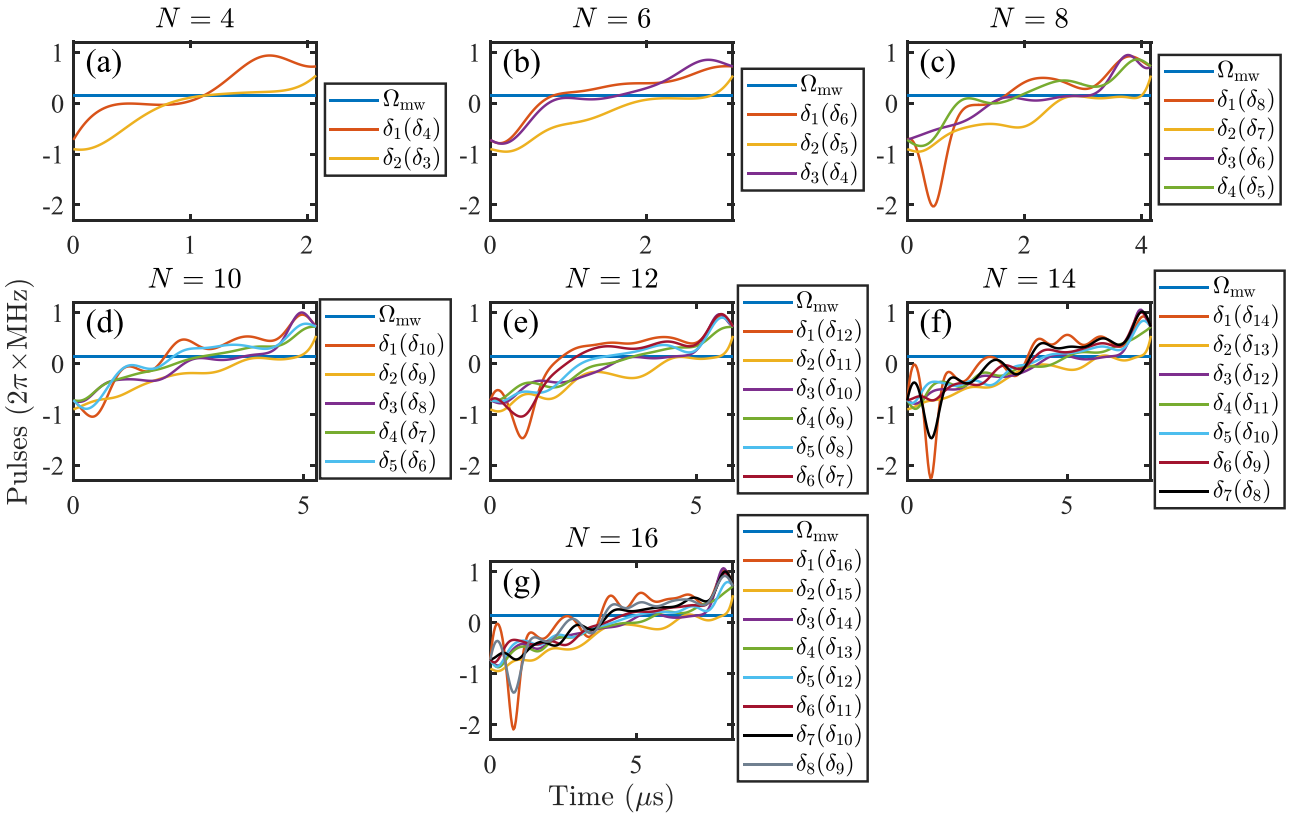

FIG. 8. Optimized microwave pulses by the GRAPE in the time domain. [(a)–(g)] The microwave pulses for systems with different sizes $N = \{4, 6, 8, 10, 12, 14, 16\}$.

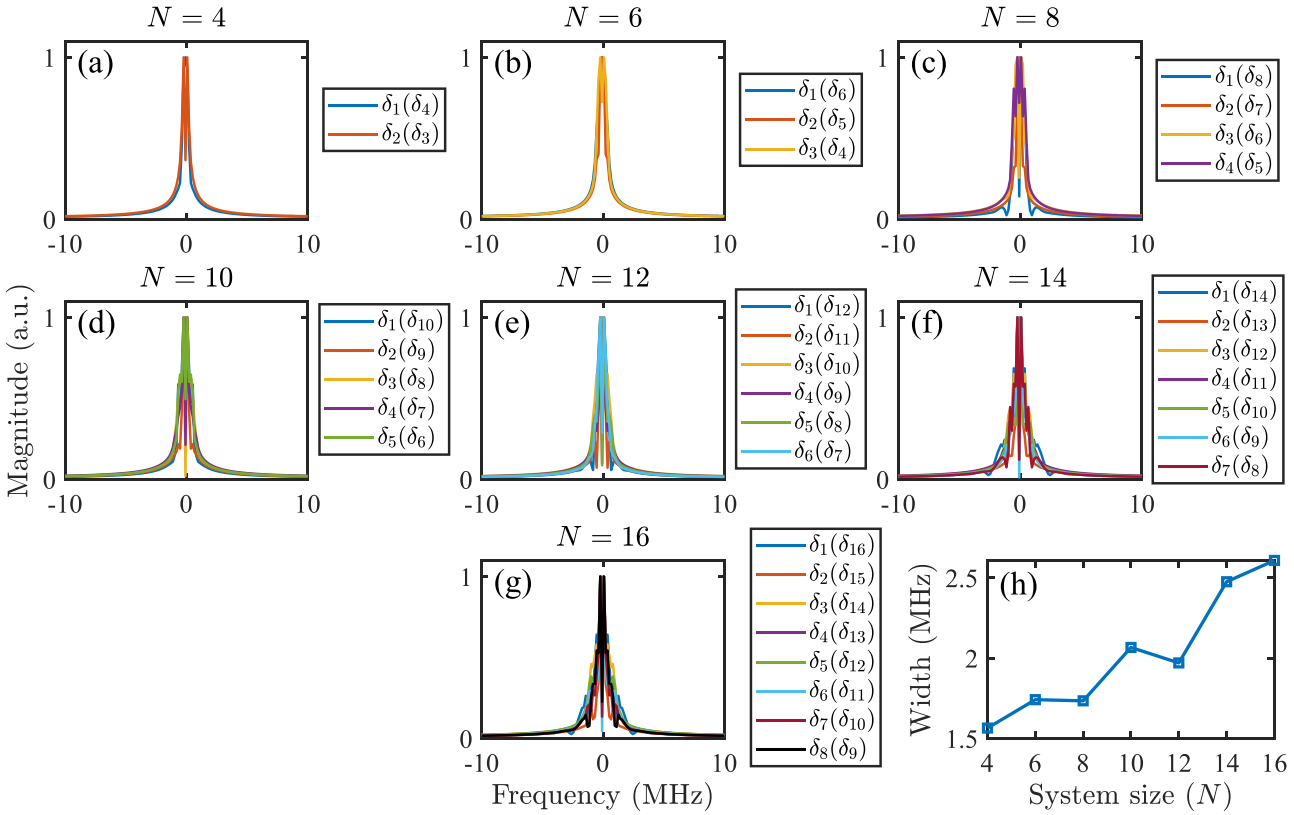

FIG. 9. Optimized microwave pulses by the GRAPE in the frequency domain. [(a)–(g)] The microwave pulses for systems with different sizes $N = \{4, 6, 8, 10, 12, 14, 16\}$. (h) Full width at $1/5$ maximum vs the system size N.

and $\Delta t = t_f/200$ are the correction strength and the time derivative, respectively.

(4) Go to step (2) until the fidelity $\mathrm{Tr}[U(t)\rho_0 U(t)^\dagger \rho_f]$ reaches a certain requirement.

The optimization results are shown in Table I in the main text. Note that the maximum absolute value of Ω_{mw} does not exceed $2\pi \times 0.14$ MHz to ensure the stability of the RDB dynamics ($J \gg \Omega_{\mathrm{mw}}$).

The optimized pulses in the time domain are shown in Fig. 8. Please note that the pulses look complicated because we place all the pulses into one subfigure. In fact, each atom has only two microwave pulses Ω_{mw} and δ^n_{mw}. All of the addressing pulses in Fig. 8 are well realized experimentally [26].

As the system size N increases, small oscillations gradually appear in the microwave pulses (see Fig. 8). To characterize these small-amplitude oscillations, we plot the pulses in the frequency domain in Fig. 9. We define frequency broadening as the full width at $1/5$ maximum (similar to the full width at half maximum) to define the frequency width. Such widths are plotted in Fig. 9(h), which gradually increases as the system size N increases. This reflects, to some extent, the difficulty of implementing such pulses experimentally because high irregular frequency microwaves usually have rising and falling edge problems. In any case, widths around 2 MHz frequency are entirely achievable using current experimental techniques [26].

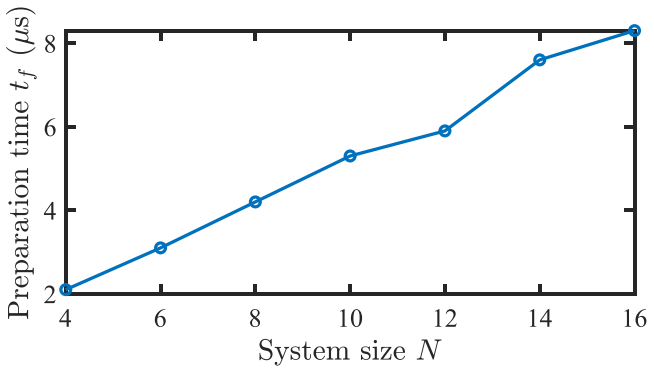

FIG. 10. Preparation time t_f of the GHZ state generation vs system size N. The curve has a trend with $t_f = N/2$ μs.

APPENDIX D: SELECTION OF THE PREPARATION TIME OF THE GHZ STATES

Specifically, we note that the preparation time t_f of the GHZ states linearly increases with system size (see Fig. 10). This is primarily because the GRAPE method constantly corrects pulses to achieve higher fidelity during optimization. As the system size increases and the degree of freedom of the system becomes larger, it becomes more difficult to find a set of nonadiabatic pulses that achieve the fidelity threshold (0.99 in this work). Therefore we appropriately increase the evolution time as the size of the system increases. A rough rule is that $t_f = N/2$ μs.

APPENDIX E: PARAMETER CHOICE OF THE SIMULATION FOR FIG. 5 IN THE MAIN TEXT

Figure 5 in the main text demonstrates the relationship between fidelities of GHZ states $\mathcal{F}$ and atomic temperature T. The selection of parameters for each temperature is different to ensure high-fidelity $\mathcal{F}$. Specifically, we choose $\{V, \Delta, |\Omega_{\rm mw}|_{\rm max}\}/(2\pi) = \{20, 7.8, 0.1\}$, $\{18, 5.5, 0.1\}$, $\{19, 5.5, 0.1\}$, $\{20, 5.5, 0.1\}$, and $\{20, 5.5, 0.1\}$ MHz for $T = 0$, 2, 4, 6, and 8 μK, respectively.

[1] M. Saffman, T. G. Walker, and K. Mølmer, Quantum information with Rydberg atoms, Rev. Mod. Phys. **82**, 2313 (2010).

[2] P. Schauß, M. Cheneau, M. Endres, T. Fukuhara, S. Hild, A. Omran, T. Pohl, C. Gross, S. Kuhr, and I. Bloch, Observation of spatially ordered structures in a two-dimensional Rydberg gas, Nature (London) **491**, 87 (2012).

[3] C. S. Hofmann, G. Günter, H. Schempp, M. Robert-de Saint-Vincent, M. Gärttner, J. Evers, S. Whitlock, and M. Weidemüller, Sub-poissonian statistics of Rydberg-interacting dark-state polaritons, Phys. Rev. Lett. **110**, 203601 (2013).

[4] S. Ebadi, T. T. Wang, H. Levine, A. Keesling, G. Semeghini, A. Omran, D. Bluvstein, R. Samajdar, H. Pichler, W. W. Ho, S. Choi, S. Sachdev, M. Greiner, V. Vuletić, and M. D. Lukin, Quantum phases of matter on a 256-atom programmable quantum simulator, Nature (London) **595**, 227 (2021).

[5] D. Bluvstein, H. Levine, G. Semeghini, T. T. Wang, S. Ebadi, M. Kalinowski, A. Keesling, N. Maskara, H. Pichler, M. Greiner, V. Vuletić, and M. D. Lukin, A quantum processor based on coherent transport of entangled atom arrays, Nature (London) **604**, 451 (2022).

[6] N. Henkel, R. Nath, and T. Pohl, Three-dimensional roton excitations and supersolid formation in Rydberg-excited Bose-Einstein Condensates, Phys. Rev. Lett. **104**, 195302 (2010).

[7] G. Pupillo, A. Micheli, M. Boninsegni, I. Lesanovsky, and P. Zoller, Strongly correlated gases of Rydberg-dressed atoms: Quantum and classical dynamics, Phys. Rev. Lett. **104**, 223002 (2010).

[8] I. Bouchoule and K. Mølmer, Spin squeezing of atoms by the dipole interaction in virtually excited Rydberg states, Phys. Rev. A **65**, 041803(R) (2002).

[9] J. E. Johnson and S. L. Rolston, Interactions between Rydberg-dressed atoms, Phys. Rev. A **82**, 033412 (2010).

[10] J. B. Balewski, A. T. Krupp, A. Gaj, S. Hofferberth, R. Löw, and T. Pfau, Rydberg dressing: Understanding of collective many-body effects and implications for experiments, New J. Phys. **16**, 063012 (2014).

[11] S. Yan, D. A. Huse, and S. R. White, Spin-liquid ground state of the $S = 1/2$ kagome Heisenberg antiferromagnet, Science **332**, 1173 (2011).

[12] L. I. R. Gil, R. Mukherjee, E. M. Bridge, M. P. A. Jones, and T. Pohl, Spin squeezing in a Rydberg lattice clock, Phys. Rev. Lett. **112**, 103601 (2014).

[13] T. Keating, K. Goyal, Y.-Y. Jau, G. W. Biedermann, A. J. Landahl, and I. H. Deutsch, Adiabatic quantum computation with Rydberg-dressed atoms, Phys. Rev. A **87**, 052314 (2013).

[14] T. Keating, R. L. Cook, A. M. Hankin, Y.-Y. Jau, G. W. Biedermann, and I. H. Deutsch, Robust quantum logic in neutral atoms via adiabatic Rydberg dressing, Phys. Rev. A **91**, 012337 (2015).

[15] M. Khazali, H. W. Lau, A. Humeniuk, and C. Simon, Large energy superpositions via Rydberg dressing, Phys. Rev. A **94**, 023408 (2016).

[16] M. Khazali, Progress towards macroscopic spin and mechanical superposition via Rydberg interaction, Phys. Rev. A **98**, 043836 (2018).

[17] Y.-Y. Jau, A. M. Hankin, T. Keating, I. H. Deutsch, and G. W. Biedermann, Entangling atomic spins with a Rydberg-dressed spin-flip blockade, Nat. Phys. **12**, 71 (2016).

[18] X. Q. Shao, D. X. Li, Y. Q. Ji, J. H. Wu, and X. X. Yi, Ground-state blockade of Rydberg atoms and application in entanglement generation, Phys. Rev. A **96**, 012328 (2017).

[19] D.-X. Li, T.-Y. Zheng, and X.-Q. Shao, Adiabatic preparation of multipartite GHZ states via Rydberg ground-state blockade, Opt. Express **27**, 20874 (2019).

[20] D. M. Greenberger, M. A. Horne, A. Shimony, and A. Zeilinger, Bell's theorem without inequalities, Am. J Phys. **58**, 1131 (1990).

[21] G. S. Agarwal, R. R. Puri, and R. P. Singh, Atomic Schrödinger cat states, Phys. Rev. A **56**, 2249 (1997).

[22] C. C. Gerry and R. Grobe, Generation and properties of collective atomic Schrödinger-cat states, Phys. Rev. A **56**, 2390 (1997).

[23] Y.-H. Chen, W. Qin, X. Wang, A. Miranowicz, and F. Nori, Shortcuts to adiabaticity for the quantum Rabi model: Efficient generation of giant entangled cat states via parametric amplification, Phys. Rev. Lett. **126**, 023602 (2021).

[24] W. Qin, A. Miranowicz, H. Jing, and F. Nori, Generating long-lived macroscopically distinct superposition states in atomic ensembles, Phys. Rev. Lett. **127**, 093602 (2021).

[25] Y.-H. Kang, Y.-H. Chen, X. Wang, J. Song, Y. Xia, A. Miranowicz, S.-B. Zheng, and F. Nori, Nonadiabatic geometric quantum computation with cat-state qubits via invariant-based reverse engineering, Phys. Rev. Res. **4**, 013233 (2022).

[26] A. Omran, H. Levine, A. Keesling, G. Semeghini, T. T. Wang, S. Ebadi, H. Bernien, A. S. Zibrov, H. Pichler, S. Choi, J. Cui, M. Rossignolo, P. Rembold, S. Montangero, T. Calarco, M. Endres, M. Greiner, V. Vuletić, and M. D. Lukin, Generation and manipulation of Schrödinger cat states in Rydberg atom arrays, Science **365**, 570 (2019).

[27] C. Song, K. Xu, H. Li, Y.-R. Zhang, X. Zhang, W. Liu, Q. Guo, Z. Wang, W. Ren, J. Hao, H. Feng, H. Fan, D. Zheng, D.-W. Wang, H. Wang, and S.-Y. Zhu, Generation of multicomponent atomic Schrödinger cat states of up to 20 qubits, Science **365**, 574 (2019).

[28] S. Ravets, H. Labuhn, D. Barredo, L. Béguin, T. Lahaye, and A. Browaeys, Coherent dipole–dipole coupling between two single Rydberg atoms at an electrically-tuned Förster resonance, Nat. Phys. **10**, 914 (2014).

[29] I. S. Madjarov, J. P. Covey, A. L. Shaw, J. Choi, A. Kale, A. Cooper, H. Pichler, V. Schkolnik, J. R. Williams, and M. Endres, High-fidelity entanglement and detection of alkaline-earth Rydberg atoms, Nat. Phys. **16**, 857 (2020).

[30] Y.-H. Kang, Y.-H. Chen, Z.-C. Shi, B.-H. Huang, J. Song, and Y. Xia, Nonadiabatic holonomic quantum computation using Rydberg blockade, Phys. Rev. A **97**, 042336 (2018).

[31] Y. Wang, C.-S. Hu, Z.-C. Shi, B.-H. Huang, J. Song, and Y. Xia, Accelerated and noise-resistant protocol of dissipation-based Knill-Laflamme-Milburn state generation with Lyapunov control, Ann. Phys. (Berlin) **531**, 1900006 (2019).

[32] S.-L. Su, F.-Q. Guo, L. Tian, X.-Y. Zhu, L.-L. Yan, E.-J. Liang, and M. Feng, Nondestructive Rydberg parity meter and its applications, Phys. Rev. A **101**, 012347 (2020).

[33] R.-H. Zheng, Y.-H. Kang, D. Ran, Z.-C. Shi, and Y. Xia, Deterministic interconversions between the Greenberger-Horne-Zeilinger states and the *W* states by invariant-based pulse design, Phys. Rev. A **101**, 012345 (2020).

[34] Y.-H. Kang, Z.-C. Shi, J. Song, and Y. Xia, Heralded atomic nonadiabatic holonomic quantum computation with Rydberg blockade, Phys. Rev. A **102**, 022617 (2020).

[35] S.-L. Su and W. Li, Dipole-dipole-interaction–driven antiblockade of two Rydberg atoms, Phys. Rev. A **104**, 033716 (2021).

[36] S. Liu, J.-H. Shen, R.-H. Zheng, Y.-H. Kang, Z.-C. Shi, J. Song, and Y. Xia, Optimized nonadiabatic holonomic quantum computation based on Förster resonance in Rydberg atoms, Front. Phys. **17**, 21502 (2022).

[37] H. Levine, A. Keesling, A. Omran, H. Bernien, S. Schwartz, A. S. Zibrov, M. Endres, M. Greiner, V. Vuletić, and M. D. Lukin, High-fidelity control and entanglement of Rydberg-atom qubits, Phys. Rev. Lett. **121**, 123603 (2018).

[38] C. L. Degen, F. Reinhard, and P. Cappellaro, Quantum sensing, Rev. Mod. Phys. **89**, 035002 (2017).

[39] W. Dür, M. Skotiniotis, F. Fröwis, and B. Kraus, Improved quantum metrology using quantum error correction, Phys. Rev. Lett. **112**, 080801 (2014).

[40] L. Egan, D. M. Debroy, C. Noel, A. Risinger, D. Zhu, D. Biswas, M. Newman, M. Li, K. R. Brown, M. Cetina, and C. Monroe, Fault-tolerant operation of a quantum error-correction code, arXiv:2009.11482v2.

[41] T. Wilk, A. Gaëtan, C. Evellin, J. Wolters, Y. Miroshnychenko, P. Grangier, and A. Browaeys, Entanglement of two individual neutral atoms using Rydberg blockade, Phys. Rev. Lett. **104**, 010502 (2010).

[42] C. Ates, T. Pohl, T. Pattard, and J. M. Rost, Antiblockade in Rydberg excitation of an ultracold lattice gas, Phys. Rev. Lett. **98**, 023002 (2007).

[43] T. Amthor, C. Giese, C. S. Hofmann, and M. Weidemüller, Evidence of antiblockade in an ultracold Rydberg gas, Phys. Rev. Lett. **104**, 013001 (2010).

[44] Z. Zuo and K. Nakagawa, Multiparticle entanglement in a one-dimensional optical lattice using Rydberg-atom interactions, Phys. Rev. A **82**, 062328 (2010).

[45] T. E. Lee, H. Häffner, and M. C. Cross, Collective quantum jumps of Rydberg atoms, Phys. Rev. Lett. **108**, 023602 (2012).

[46] W. Li, C. Ates, and I. Lesanovsky, Nonadiabatic motional effects and dissipative blockade for Rydberg atoms excited from optical lattices or microtraps, Phys. Rev. Lett. **110**, 213005 (2013).

[47] S.-L. Su, E. Liang, S. Zhang, J.-J. Wen, L.-L. Sun, Z. Jin, and A.-D. Zhu, One-step implementation of the Rydberg-Rydberg-interaction gate, Phys. Rev. A **93**, 012306 (2016).

[48] N. Rach, M. M. Müller, T. Calarco, and S. Montangero, Dressing the chopped-random-basis optimization: A bandwidth-limited access to the trap-free landscape, Phys. Rev. A **92**, 062343 (2015).

[49] R. Heck, O. Vuculescu, J. J. Sørensen, J. Zoller, M. G. Andreasen, M. G. Bason, P. Ejlertsen, O. Elíasson, P. Haikka, J. S. Laustsen, L. L. Nielsen, A. Mao, R. Müller, M. Napolitano, M. K. Pedersen, A. R. Thorsen, C. Bergenholtz, T. Calarco, S. Montangero, and J. F. Sherson, Remote optimization of an ultracold atoms experiment by experts and citizen scientists, Proc. Natl. Acad. Sci. USA **115**, E11231 (2018).

[50] N. Khaneja, T. Reiss, C. Kehlet, T. Schulte-Herbrüggen, and S. J. Glaser, Optimal control of coupled spin dynamics: Design of NMR pulse sequences by gradient ascent algorithms, J. Magn. Reson. **172**, 296 (2005).

[51] L. Hu, Y. Ma, W. Cai, X. Mu, Y. Xu, W. Wang, Y. Wu, H. Wang, Y. P. Song, C.-L. Zou, S. M. Girvin, L.-M. Duan, and L. Sun, Quantum error correction and universal gate set operation on a binomial bosonic logical qubit, Nat. Phys. **15**, 503 (2019).

[52] Y. Ma, Y. Xu, X. Mu, W. Cai, L. Hu, W. Wang, X. Pan, H. Wang, Y. P. Song, C.-L. Zou, and L. Sun, Error-transparent operations on a logical qubit protected by quantum error correction, Nat. Phys. **16**, 827 (2020).

[53] Y. Ma, X. Pan, W. Cai, X. Mu, Y. Xu, L. Hu, W. Wang, H. Wang, Y. P. Song, Z.-B. Yang, S.-B. Zheng, and L. Sun, Manipulating complex hybrid entanglement and testing multipartite Bell inequalities in a superconducting circuit, Phys. Rev. Lett. **125**, 180503 (2020).

[54] Y. Xu, Y. Ma, W. Cai, X. Mu, W. Dai, W. Wang, L. Hu, X. Li, J. Han, H. Wang, Y. P. Song, Z.-B. Yang, S.-B. Zheng, and L. Sun, Demonstration of controlled-phase gates between two error-correctable photonic qubits, Phys. Rev. Lett. **124**, 120501 (2020).

[55] A. Omran (private communication).

[56] S. de Léséleuc, D. Barredo, V. Lienhard, A. Browaeys, and T. Lahaye, Analysis of imperfections in the coherent optical excitation of single atoms to Rydberg states, Phys. Rev. A **97**, 053803 (2018).

[57] J.-L. Wu, Y. Wang, J.-X. Han, S.-L. Su, Y. Xia, Y. Jiang, and J. Song, Resilient quantum gates on periodically driven Rydberg atoms, Phys. Rev. A **103**, 012601 (2021).

[58] I. I. Beterov, I. I. Ryabtsev, D. B. Tretyakov, and V. M. Entin, Quasiclassical calculations of blackbody-radiation-induced depopulation rates and effective lifetimes of Rydberg *nS*, *nP*, and *nD* alkali-metal atoms with $n \leqslant 80$, Phys. Rev. A **79**, 052504 (2009).